

Topological surface currents accessed through reversible hydrogenation of the three-dimensional bulk

Haiming Deng¹, Lukas Zhao¹, Kyungwha Park², Jiaqiang Yan³, Kamil Sobczak⁴,
and Lia Krusin-Elbaum^{1,5†}

¹Department of Physics, The City College of New York - CUNY, New York
10031, USA

²Department of Physics, Virginia Tech, Blacksburg, Virginia 24061, USA

³Materials Science and Technology Division, Oak Ridge National Laboratory, Oak
Ridge, Tennessee 37831, USA

⁴Faculty of Chemistry, Biological and Chemical Research Center, University of
Warsaw, 02-089 Warsaw, Poland

⁵City University of New York Graduate Center, New York, New York 10016, USA

Hydrogen, the smallest and most abundant element in nature, can be efficiently incorporated within a solid and drastically modify its electronic state — it has been known to induce novel magnetoelectric effects in complex perovskites and modulate insulator-to-metal transition in a correlated Mott oxide. Here we demonstrate that hydrogenation resolves an outstanding challenge in chalcogenide classes of three-dimensional (3D) topological insulators and magnets — the control of intrinsic bulk conduction that denies access to quantum surface transport. With electrons donated by a reversible binding of H⁺ ions to Te(Se) chalcogens, carrier densities are easily changed by over 10^{20} cm⁻³, allowing tuning the Fermi level into the bulk bandgap to enter surface/edge current channels. The hydrogen-tuned topological materials are stable at room temperature and tunable disregarding bulk size, opening a breadth of platforms for harnessing emergent topological states.

The ability to control carrier density — a key parameter of the electronic state of condensed matter — is central to achieving access to the topologically protected surface states in three-dimensional (3D) topological materials (TIs) that ideally are insulating in the bulk (*1*). In the absence of magnetic dopants, the 2D electronic surface states with Dirac-type (linear) energy-momentum dispersion (*1*) are gapless and fully spin-polarized, with protection against backscattering by local disorder guaranteed by time-reversal symmetry. These important layered van der Waals (vdW) quantum materials have narrow ($\simeq 300$ meV) bulk gaps (*2*) and charge carriers donated by intrinsic lattice defects (*3*). As a result, bulk conduction can dominate the surface channels, hindering the studies of the Dirac states and their implementation in topological spintronics and fault-tolerant quantum computing (*4*).

Recent realizations of a nontrivial quantum anomalous Hall (QAH) state, featuring dissipation-free chiral edge currents (*5*), made it apparent that when long-range magnetism and band topology combine (*6*) the problem of bulk conduction can be particularly acute. Magnetic dopants, by breaking time-reversal symmetry, gap out the Dirac surface channels (*7*), and when the Fermi level is in the Dirac (mass) gap the QAH state is expected to emerge. However, in addition to magnetic moment, the dopants also donate charge. Indeed, QAH was first observed in heavily Cr-doped $(\text{Bi,Sb})_2\text{Te}_3$ ultrathin films (*8*) in which to minimize bulk conduction a non-stoichiometric alloying of the constituent elements was employed and the film thickness had to be precisely controlled. Moreover, doping disorder restricted QAH temperature to the mK range.

In a newly discovered important class of intrinsic topological magnets (ITM) (*9*) the doping and alloying disorders are avoided because the magnetic dopants are arranged as an atomic layer in a layered van der Waals (vdW) crystal structure. For example, the Mn-based ITM MnBi_2Te_4 consists of Te-Bi-Te-Mn-Te-Bi-Te septuple layers (SLs), separated by vdW gaps and coupled antiferromagnetically (*10*). As a consequence, the anomalous Hall (near) quantization was observed at higher temperatures (*11*). However, such materials show high bulk carrier densities (typically $> 10^{20} \text{ cm}^{-3}$) (*12, 13*), and observation of QAH required delicate tuning of charge density that was again only possible in ultrathin (3-5 nm) samples with odd number of SLs. In thicker (hundreds of nanometers) samples ferromagnetism and quantization could be achieved when SLs were separated by a topological spacer (*14*), yet tuning to quantization of either ferromagnetic (FM) or antiferromagnetic (AFM) ITMs without imposing severe thickness constraints is a major obstacle to realizing novel topological quantum states.

Here we demonstrate a remarkably efficient and facile way to reversibly tune bulk carrier densities by over $\simeq 10^{20} \text{ cm}^{-3}$ in different classes of layered topological materials by using insertion and extraction of ionic hydrogen to achieve access to topological surface states. The source of H^+ ions is a dilute aqueous hydrochloric acid (HCl) solution, which leaves the TI crystal structure intact and has an extra benefit of removing native surface oxide while passivating surfaces and preventing reox-

idation under exposure to air. We show that H^+ in TIs, by preferentially forming an H-Te(Se) moiety within van der Waals gaps, donates electrons to the system and moves Fermi level from the bulk-valence (BVB) to bulk-conduction (BCB) bands, crossing the bulk bandgap to display an ambipolar p - to n -type conductance conversion at the charge neutrality point. The process is fully reversible, as hydrogen-chalcogen moiety can be disassociated by a low-temperature annealing protocol under which hydrogen is easily removed. It is also multiply-cyclable and reproducible, thereby resolving one of the key limitations of magnetic and nonmagnetic TIs.

Generally, crystal growth of tetradymite crystals such as Bi_2Te_3 and Bi_2Se_3 results in equilibrium defect configurations comprising vacancies and antisites on different sublattices (3). In undoped Bi_2Se_3 , where Se vacancies tend to dominate, the net conduction is by electron carriers or n -type. In Bi_2Te_3 , where antisites are prevalent (15) the conductivity is usually p -type, namely by hole carriers, although by varying stoichiometry it has been grown of either conductivity type. Exploring growth and the exact doping/alloying conditions for the Fermi level E_F to lie within the narrow bulk gap is a lengthy and often chancy process. By contrast, we show that a post-growth hydrogenation can tune E_F to charge neutrality in hours, and can be effective in single crystals and in nano-devices, where the evolution of resistance under hydrogenation is easily monitored over time.

The ultralight hydrogen diffuses rapidly and easily incorporates into many materials (16), although it shows qualitatively different behavior in different hosts (17). It has been shown to modify both electronic and structural states (18–21) — turning graphene into graphane (20), inducing new magnetic phases in complex perovskites (21) and modulating insulator-to-metal transition in a correlated Mott oxide VO_2 (22). In most semiconductors interstitial hydrogen binds to defects (17) and is known to be amphoteric (23), namely it can act either as a donor (H^+) or an acceptor (H^-) of charge, nearly always counteracting the prevailing conductivity type. To ascertain the effects of hydrogen uptake on charge transport in the topological materials we first chose well characterized Bi_2Te_3 crystals with the conductivity flavor initially of a net acceptor type. The level of hydrogenation was controlled by timing the diffusion of H^+ ions from a dilute (0.5 molar) $HCl + H_2O = H^+(H_2O) + Cl^-$ solution maintained at room temperature in which the samples were immersed for a period of minutes to hours (see Figs. 1A,B and Materials and Methods).

Our key and a most immediately notable result shown in Figure 1 is a nearly two orders of magnitude increase in the low-temperature longitudinal resistance R_{xx} as a function of HCl exposure time to a maximum R_{xx}^{\max} and a subsequent decrease as the exposure time is prolonged (Fig. 1C). The resistance maximum R_{xx}^{\max} (conductance minimum) is at the charge-neutral point (CNP) where conduction is converted from p - to n -type, as determined from the corresponding Hall resistance (Fig. 1D). We surmise then that hydrogen, through the process of in-diffusion into the bulk (see Supplementary Note 1), indeed donates electrons. This process is not self-limiting: at long (≥ 24 h)

exposure times a decrease in R_{xx} on the deep n -side slows down yet continues. The observed ambipolar conduction, with well-distinguished p (hole) and n (electron) conduction regions, can be reproducibly reversed when hydrogen is removed by a low-temperature anneal (sketch in Fig. 1B) in the easily accessible range that depends on sample thickness. For the ~ 200 nm thick Bi_2Te_3 crystal shown here the de-hydrogenation and a return from n -type across the CNP back to p -type is obtained within $\sim 100^\circ\text{C}$. Importantly, the carrier mobility during the entire process is not affected — e.g. in the sample in Fig. 1 it remains at $\cong 7,000 \text{ cm}^2\text{V}^{-1}\text{s}^{-1}$ (Supplementary Table 1).

After each annealing step the system is room-temperature stable and can be further finetuned by the conventional electrostatic gating. Figure 1E shows that once the carrier density is sufficiently reduced by H^+ , the vicinity of the CNP can be reproducibly explored by applying a gate voltage V_g . $R_{xx}(V_g)$ is precisely reversible upon changing the direction of the V_g sweep — the absence of hysteresis is a clear indication that hydrogenation does not create surface traps (24) and is consistent with hydrogen permeating the bulk. We emphasize that in thick (≥ 100 nm) materials, far away from the CNP where carrier densities are in the high $\sim 10^{19} \text{ cm}^{-3}$ range, the CNP can not be reached by gating within a practically accessible voltage sweep (Fig. 1F).

The type conversion on hydrogenation and de-hydrogenation is clearly seen in the magnetic field dependence of Hall resistance R_{xy} (Fig. 2A), with R_{xy} flipping its slope dR_{xy}/dH and Hall coefficient $R_H = -\frac{1}{nbe}$ changing sign in the conversion region. Figure 2B shows a characteristic low-field ambipolar behavior of R_{xy} near the CNP, where the net residual bulk carrier density is very low. As we approach the CNP, weak antilocalization (WAL) quantum correction to ‘classical’ conductivity emerges at low magnetic fields as a *positive* magnetoresistance cusp (Fig. 2C), characteristic of a TI (25). The number n_Q of quantum conduction channels contributing to WAL can be estimated from 2D localization theory (26) $\Delta G(B) \simeq \alpha \frac{e^2}{2\pi^2\hbar} f(\frac{B_\phi}{B})$, where $\Delta G(B)$ is the low-field quantum correction to 2D magnetoconductance, coefficient $\alpha = n_Q/2$ equals to 1/2 for a single 2D channel, $f(x) \equiv \ln x - \psi(1/2 + x)$, ψ is the digamma function, and field $B_\phi = \frac{\hbar}{4el_\phi^2}$ is related to the dephasing length l_ϕ of interfering electron paths. The fit to WAL conductance (see Supplementary Fig. 1) yields $\alpha \simeq 1.004 \pm 0.001$, corresponding to two 2D quantum channels we associate with top and bottom topological surfaces (25). Figure 2D schematically depicts the Bi_2Te_3 bandstructure (2) as the Fermi level E_F moves from BVB to BCB (hydrogen in) and in reverse (hydrogen out). The 2D WAL cusp is seen when E_F is within the Dirac bands.

The change in the net carrier density induced by hydrogenation is reflected in the Shubnikov-de Haas (SdH) quantum oscillations of Hall resistance at higher fields (Fig. 2B). An estimate of the Fermi surface size obtained from the change of the oscillation period in $\delta R_{xy}/\delta\mu_0 H$ (Fig. 2E-G) shows that the Fermi vector k_F is much reduced after hydrogenation (Supplementary Table 2) — near the CNP $k_F \approx 0.014 \text{ \AA}^{-1}$ and the corresponding carrier density $n \cong \times 10^{16} \text{ cm}^{-3}$ is very low.

After a longer time exposure (5.8 h) to HCl, as E_F enters BCB the Fermi surface size becomes large again, albeit a more complex one (with three oscillation periods, see Fig. 2, Supplementary Fig. 2), reflecting the Bi_2Te_3 bandstructure with n -type Dirac bands mixing with BVB.

Next we ask, where does hydrogen go? Our transport experiments demonstrate that in Bi_2Te_3 hydrogen donates electrons and stabilizes in its positive charge state as H^+ , a proton. To optimize its Coulomb interaction with the host electrons, it will tend to locate in the regions of higher electron charge density, i.e. in the vicinity of a more electronegative Te. To chase its physical presence we first utilize time-of-flight secondary ion mass spectrometry (ToF-SIMS), focusing on Te (Figs. 3A-D, Supplementary Fig. 3). A negative bias mass spectrum of secondary ions (see Materials and Methods) ejected from Bi_2Te_3 shows a cluster of peaks in the 120-130 u (atomic mass) range (Fig. 3C) that belong to several naturally occurring isotopes of Te, see Supplementary Table 3. A closer look at the Te isotope cluster (Fig. 3D) clearly shows additional peaks that differ from each Te isotope by exactly $\Delta u = 1$, consistent with each isotope binding with one hydrogen.

On a microscopic scale, we confirm the affinity between H and Te by x-ray photoelectron spectroscopy (XPS), see Methods. XPS spectra near the Bi 4f and Te 3d core levels show that, despite a strong doping effect of hydrogen, the Bi core levels (27) are unperturbed (Fig. 3E), while the spectral shapes of Te 3d peaks are quantifiably modified (Fig. 3F,G). The upshift $\Delta = 1$ eV in binding energy due to $[\text{Te-H}]^-$ moiety is easily distinguished from free hydrogen or surface oxidation, as seen, for example, during hydrogen electro-catalysis (28), where Bi 4f spectral shapes are upshifted by ~ 2 eV and both Bi_2O_3 and TeO_2 peaks are present. By contrast, XPS shows that surface oxide is cleanly removed by HCl, and that Cl is entirely absent (Supplementary Fig. 4 and Table 4).

The electron-donor action of hydrogen in a vdW TI through formation of hydrogen-chalcogen moiety is borne out by the density functional theory (DFT) calculations (see Supplementary Note 2 and Supplementary Figs. 5-7). The calculated band structures of Bi_2Te_3 (Fig. 4A-C) show that after hydrogenation the Dirac bands are preserved while the Fermi level E_F is upshifted into the BCB. This n -type doping is independent of whether H^+ goes in interstitially or into the van der Waals gaps, however the H-Te moiety appears most stable within the vdW gap (the formation energies are in line with XPS). The calculated local density of states (DOS) (Fig. 4D) highlights the shift of E_F relative to the Dirac point (DP). Bi_2Te_3 structure maintains charge balance within each quintuple layer (QL) of atoms $\text{Te}^{(1)}\text{-Bi}\text{-Te}^{(2)}\text{-Bi}\text{-Te}^{(1)}$, where the superscripts distinguish the inequivalent Te sites (see Supplementary Fig. 6a). The Te-Bi bonds are polar-covalent while only weak vdW type bonding exists between the neighboring $\text{Te}^{(1)}\text{-Te}^{(1)}$ planes with relatively weak and highly polarizable bonds. The hydrogen prefers going to the region between these planes (Fig. S7), while the crystal structure remains intact (Supplementary Fig. 8).

The Fermi level tuning by hydrogenation demonstrated here is very general, indeed it is remark-

ably effective in other chalcogen-based TI. We have achieved the type conversion across the CNP in Se-containing materials, such as $\text{Bi}_2\text{Te}_2\text{Se}$ (Supplementary Fig. 9) and Ca-doped Bi_2Se_3 (Supplementary Figs. 10,11). Our DFT calculations confirm that a stable $[\text{H-Se}]^-$ moiety similarly acts to move the Fermi level towards the conduction bands (Supplementary Figs. 6,7).

The technique is also very powerful in magnetic TI, and particularly in a very promising ITM class. One example is the intrinsic ferromagnetic $\text{MnBi}_2\text{Te}_4/\text{Bi}_2\text{Te}_3$ superlattice (14) where initial bulk carrier density is in the 10^{20} cm^{-3} range, yet type conversion across the CNP by hydrogen is obtained (Supplementary Figs. 12,13). Hydrogenation can also deliver an essentially continuous E_F tuning across the bulk gap of an intrinsic topological antiferromagnet, where the axion insulator behavior was very recently reported when the antiferromagnetic ITM was made thin enough (~ 6 SLs or ~ 8 nm) (29) to reduce the contribution from bulk conduction channels and to be able to deplete bulk carriers by electrostatic gating. We demonstrate that through hydrogen-tuning of E_F we can turn the bulk AFM ITM into an insulating state sans voltage gating. Figure 4E shows how the longitudinal resistance $R_{xx}(T)$ of a ten times thicker $\text{MnBi}_{2-x}\text{Sb}_x\text{Te}_4$ ($x = 0.6$) crystal continuously transforms under hydrogenation from a metallic-like into a strongly insulating-like — a feat not achieved by a step-wise Bi-Sb alloying (12). Under hydrogen uptake the Néel temperature $T_N \sim 25 \text{ K}$ remains unchanged while the low-temperature $R_{xx}(T)$ increases by about two orders of magnitude, reaching maximum value at the CNP (Fig. 4F). The Hall resistance R_{xy} (Fig. 4G) at the CNP displays ambipolar behavior, akin to the one in Bi_2Te_3 (Fig. 1D). The field dependencies of $R_{xx}(H)$ and $R_{xy}(H)$ under hydrogenation are consistent with the results in thin flakes under voltage gating (11, 29), also see Supplementary Fig. 14. Near the CNP the magnetoresistance $R_{xx}(H)$ sharply changes at two characteristic fields: H_1 , above which the spin order is driven into a canted AFM state (12,13), and H_2 at which all spins align in a FM state (Fig. 4H). Below H_1 , Hall resistance $R_{xy}(H)$ exhibits a distinct plateau (where some of the SLs align with field) and a ‘zero-plateau’ (Fig. 4I). Together with the rapidly decreasing $R_{xx}(H_1 < H < H_2)$ these are the key signatures of surface currents in close proximity to the Chern (30) and axion (31) insulator states.

Finally, we remark that a paucity of bulk-insulating topological materials significantly impedes the search for emergent topological quantum phenomena, with the prospect for real-world applications remaining far off. Hydrogen-tunability of high bulk carrier densities expands the availability of robust and easily accessible platforms for observing and harnessing distinct topological phases with stunning macroscopic manifestations, such as dissipationless edge transport of charge and axion electrodynamics (30) in topological magnets. It should facilitate the search for quantized magnetoelectric (32) and magneto-optical (33) effects, and could lead to higher-temperature and higher-order topological states for future antiferromagnetic spintronics (34) and quantum computing.

References and Notes

1. X.-L. Qi, S.-C. Zhang, *Rev. Mod. Phys.* **83**, 1057 (2011).
2. H. Zhang, *et al.*, *Nature Phys.* **5**, 438 (2009).
3. D. Scanlon, *et al.*, *Adv. Mater.* **24**, 2154 (2012).
4. M. He, H. Sun, Q. He, *Front. Phys.* **14**, 43401 (2019).
5. C.-X. Liu, S.-C. Zhang, X.-L. Qi, *Annu. Rev. Condens. Matter Phys.* **7**, 301–21 (2016).
6. Y. Tokura, K. Yasuda, A. Tsukazaki, *Nature Rev. Phys.* **1**, 126 (2019).
7. Y. Chen, *et al.*, *Science* **329**, 659 (2010).
8. C.-Z. Chang, *et al.*, *Science* **340**, 167–170 (2013).
9. J. Li, *et al.*, *Sci. Adv.* **5**, eaaw5685 (2019).
10. M. Otrokov, *et al.*, *Nature* **576**, 416 (2019).
11. Y. Deng, *et al.*, *Science* **367**, 895 (2020).
12. J.-Q. Yan, *et al.*, *Phys. Rev. B* **100**, 104409 (2019).
13. B. Chen, *et al.*, *Nature Comms.* **10**, 4469 (2019).
14. H. Deng, *et al.*, *Nature Phys.* **17**, 36 (2021).
15. C. Drašar, P. Lošták, C. Uher, *J. Electronic Mat.* **39**, 2162 (2010).
16. L. Schlapbach, A. Züttel, *Nature* **414**, 353 (2001).
17. S. Myers, *et al.*, *Rev. Mod. Phys.* **64**, 559–617 (1992).
18. H. Yoon, *et al.*, *Nature Mater.* **15**, 1113 (2016).
19. J. Shi, Y. Zhou, S. Ramanathan, *Nature Comm.* **5**, 4860 (2014).
20. D. Elias, *et al.*, *Science* **323**, 610 (2009).
21. N. Lu, *et al.*, *Nature* **546**, 124 (2017).
22. K. Shibuya, A. Sawa, *Adv. Electron. Mater.* **2**, 1500131 (2016).
23. C. Van de Walle, J. Neugebauer, *Annu. Rev. Mater. Res.* **36**, 179 (2006).
24. E. Papalazarou, *et al.*, *Phys. Rev. Materials* **2**, 104202 (2018).
25. L. Zhao, *et al.*, *Nature Comm.* **7**, 10957 (2016).
26. S. Hikami, A. Larkin, Y. Nagaoka, *Progress Theor. Phys.* **63**, 707 (1980).
27. P. Kumar, *et al.*, *J. Phys. D: Appl. Phys.* **46**, 285301 (2013).
28. Q. Qu, *et al.*, *ACS Catal.* **10**, 2656 (2020).
29. C. Liu, *et al.*, *Nature Mater.* **19**, 522 (2020).
30. X. L. Qi, T. L. Hughes, S. C. Zhang, *Phys. Rev. B* **78**, 195424 (2008).

31. D. Zhang, *et al.*, *Phys. Rev. Lett.* **122**, 206401 (2019).
32. J. Wang, B. Lian, X. Qi, S. Zhang, *Phys. Rev. B* **92**, 081107 (2015).
33. W. Feng, *et al.*, *Nature Comms.* **11**, 118 (2020).
34. L. Smejkal, Y. Mokrousov, B. Yan, A. MacDonald, *Nature Phys.* **14**, 242 (2018).

Acknowledgements: We wish to thank Tai-De Li for the technical assistance with the surface analytical tools at the Surface Science Facility of CUNY Advanced Science Research Center (ASRC). Jim Hone’s probing comments are much appreciated. This work was supported by the NSF grants DMR-1420634, DMR-2011738, and HRD-1547830. Computational support was provided by Virginia Tech ARC and San Diego Supercomputer Center (SDSC) under DMR-060009N.

Author Contributions Experiments were designed by H.D. and L.K.-E.. Materials were grown by H.D. and J.Y., and their modification and characterization, device fabrication and transport measurements were performed by H.D. and L.Z.. HAADF-STEM and EDX elemental imaging was performed by K.S.. DFT bandstructures and electronic density of states (DOS) under hydrogenation were calculated by K.P.. Data analysis was done by H.D. and L.K.-E. L.K.-E. wrote the manuscript with the input from H.D. [†]Correspondence should be addressed to L. K.-E (email: lkrsin@ccny.cuny.edu).

FIGURE LEGENDS

Fig. 1. Tuning bulk conductivity of a topological material by hydrogenation. **A,B**, Illustration of hydrogenation and de-hydrogenation process. **A**, Hydrogenation: sample is submerged in a dilute aqueous HCl solution (0.5M) at room temperature where H^+ permeates the bulk through a timed diffusion process. **B**, De-hydrogenation: H^+ inside the sample is controllably released as H_2 gas by an anneal in the 70 – 200°C temperature range prescribed by the sample thickness. **C**, Longitudinal resistance R_{xx} and **D**, Hall resistance R_{xy} at 2 K and -5.7 T of the initially p -type Bi_2Te_3 120nm-thick exfoliated device *vs.* hydrogenation time (bottom axis) show conversion (following blue arrows) to n -type (blue symbols). The back-conversion (red symbols) to p -type (following red arrows) is controlled by thermal annealing steps (30 min at each temperature, top red axis). R_{xx} increases by nearly two orders of magnitude at the \sim CNP. The maximum is at the ambipolar point in R_{xy} . *Top inset:* Bi_2Te_3 bandstructure rendering. *Bottom inset:* Optical image of the sample with van der Pauw contact geometry used. **E**, Electrostatic back-gating in the vicinity of the CNP (labeled **1**) reveals the expected maximum in R_{xx} at the CNP. The non-hysteretic R_{xx} *vs.* gating voltage V_g indicates an absence of surface traps. **F**, Far from the CNP on the n -type (labeled **2**) or p -type side (labeled **3**), the R_{xx} maximum is inaccessible by voltage gating.

Fig. 2. Transport and quantum oscillations across charge neutrality point. **A**, Hall resistance R_{xy} *vs.* magnetic field H after hydrogenation and on annealing at different temperatures T_a . Initially, the pristine Bi_2Te_3 crystal is p -type. The conversion from p - to n -type and back is indicated by the sign change of the slope dR_{xy}/dH . **B**, In the compensated region near the CNP there are both carrier types from the surfaces and the bulk. At higher fields Hall slope is negative and SdH oscillations are observed, as expected from the n -type Dirac surface states (see Fig. 2D). *Inset:* nonlinear Hall resistance near zero field. **C**, Evolution of magnetoresistance (normalized to the value at zero field) under annealing with time steps $\Delta t = 30$ min implemented to tune Bi_2Te_3 crystal to stable CNP; it evolves from a quadratic field dependence of a typical bulk metal to a weak antilocalization (WAL) regime with a characteristic low-field cusp near CNP. The cusp fit parameter $\alpha = 2 \times 0.5$ signifies

contributions from top and bottom surfaces (0.5 from each), see text and Supplementary Fig. 1. **D**, Bandstructure cartoon for Bi_2Te_3 illustrates the upshift of the Fermi level E_F on hydrogenation (cyan arrow) and the reversal by de-hydrogenation (red arrow). In Bi_2Te_3 , the E_F^0 at the CNP is slightly above the Dirac point (DP) ($I, 2$). Shubnikov-de Haas (SdH) quantum oscillations of $\delta R_{xy}/\mu_0\delta H$ in Bi_2Te_3 with magnetic field applied along the c -axis: **E**, before hydrogenation, **F**, near the CNP and **G**, after 5.8 h exposure to H^+ . The corresponding sizes of Fermi surfaces are drawn as circles.

Fig. 3. Spectroscopic detection of hydrogen in Bi_2Te_3 . **A**, Time-of-flight secondary ion mass spectrometry (ToF-SIMS) generates mass spectrum of the outermost 1.5-2.0 nm surface region by bombarding it with a primary ion (Bi^+) beam. **B**, ToF-SIMS images of Te (*left*), Bi (*middle*), and Si substrate (*right*) indicate the rastered area from which the spectra were obtained (see Methods). The scale bar is 10 μm . **C**, Mass analysis of the secondary ions under negative bias shows the presence of ^1H , ^{128}Te , ^{209}Bi , and $^{129}[\text{Te-H}]$ moieties. Well separated peaks of the known long-lived Te isotopes with the intensity ratios occurring in nature (Supplementary Table 3) are detected. **D**, The expanded view of the Te isotope atomic mass range clearly shows additional peaks (highlighted in blue) of lower intensity that perfectly and sequentially follow each Te^α peak by precisely $\Delta u = 1$. Some hydrogen peaks appear to overlap with Te^α . **E**, XPS data of Bi $4f_{7/2}$ and $4f_{5/2}$ for pristine Bi_2Te_3 and H^+ treated for $t = 12$ hours show no change after hydrogenation. **F**, Te $3d_{3/2}$ and $3d_{5/2}$ are modified by hydrogenation. **G**, Analysis of the Te $3d$ XPS peaks clearly shows H binding to Te with a shift in binding energy of $\Delta = 1\text{eV}$.

Fig. 4. DFT-calculated bandstructures under hydrogenation and hydrogen-induced conductivity type conversion in a magnetic TI. DFT bandstructures for four quintuple layer (QL) slabs of **A**, pristine Bi_2Te_3 , **B**, with interstitial hydrogen ($\text{H-Te}^{(2)}$ bonding) within QLs and **C**, with hydrogen in the vdW gap ($\text{H-Te}^{(1)}$ bonding). The red color indicates the states localized at the top or bottom surface states. **D**, Calculated total electronic densities of states (DOS). *Top*: For pristine Bi_2Te_3 . *Middle*: With hydrogen in the vdW gaps acting as electron donor. *Bottom*: Cl would act as electron acceptor, moving E_F in the opposite direction — the doping action not observed experimentally in transport and consistent with the absence of Cl in XPS. **E**, Longitudinal resistance $R_{xx}(T)$ of a ~ 80 nm thick $\text{MnBi}_{2-x}\text{Sb}_x\text{Te}_4$ ($x = 0.6$) crystal clearly shows hydrogen-induced transformation from a metallic to an insulator-like state. Inset: The characteristic cusp (red arrow) occurs at the Néel temperature $T_N \sim 25$ K, which is not affected by hydrogenation. **F**, Longitudinal resistance R_{xx} and **G**, Hall resistance R_{xy} of the same crystal at 1.9 K (below T_N), both as a function of hydrogenation time and annealing temperature T_a . The maximum of R_{xx} is at the CNP where the conduction is converted from p - to n -type, and correspondingly the ambipolar behavior is observed in R_{xy} . **H**, R_{xx} and **I**, Hall resistance R_{xy} at 1.9 K measured at the CNP as a function of applied magnetic field. Below T_N and above the characteristic field $H_1 \approx 3$ T (green arrows) the system is driven into a canted AFM state, and becomes fully FM aligned at $H_2 \approx 6$ T (black arrows). The surface Hall currents switch from a zero R_{xy} plateau to a finite plateau when some of the SLs align with the field. The R_{xy} plateaus observed below H_1 are hallmark signatures of the Chern and axion insulator states.

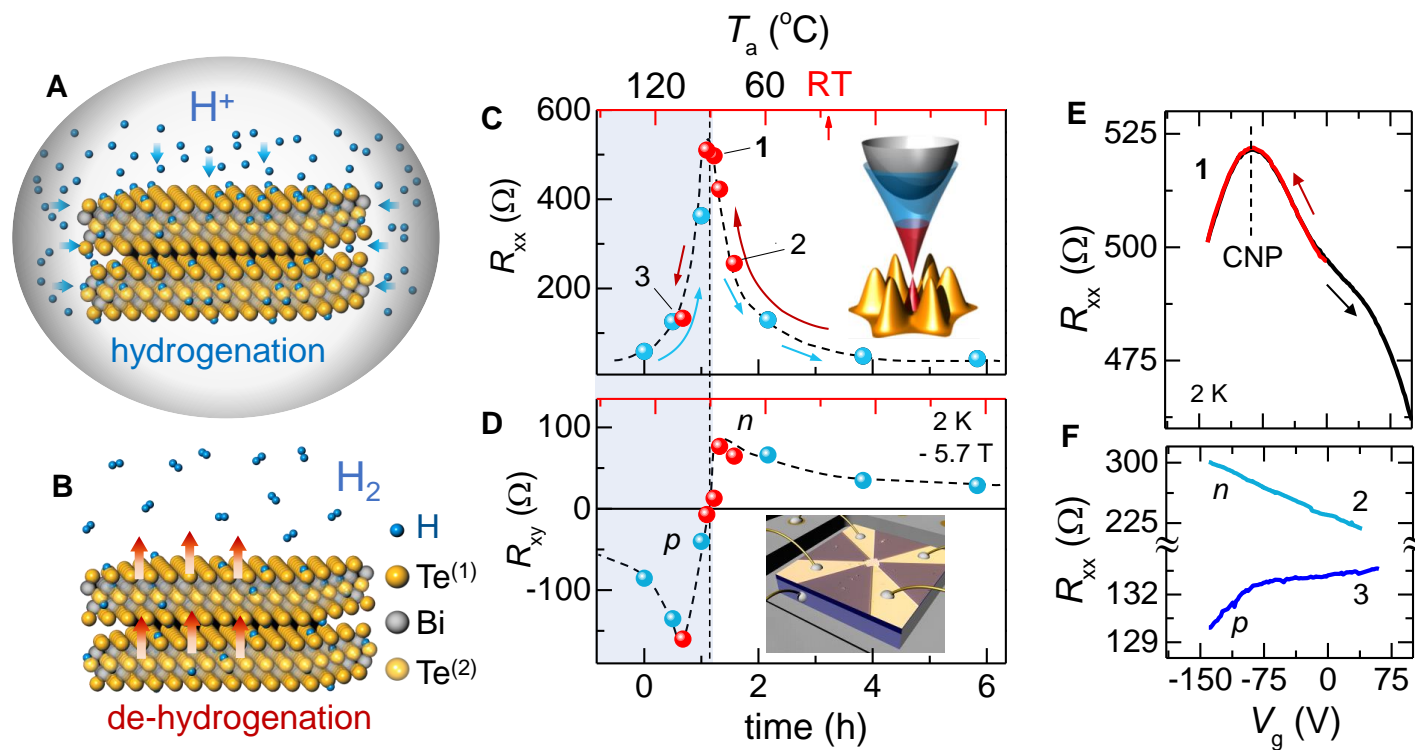


Fig. 1; HD *et al.*

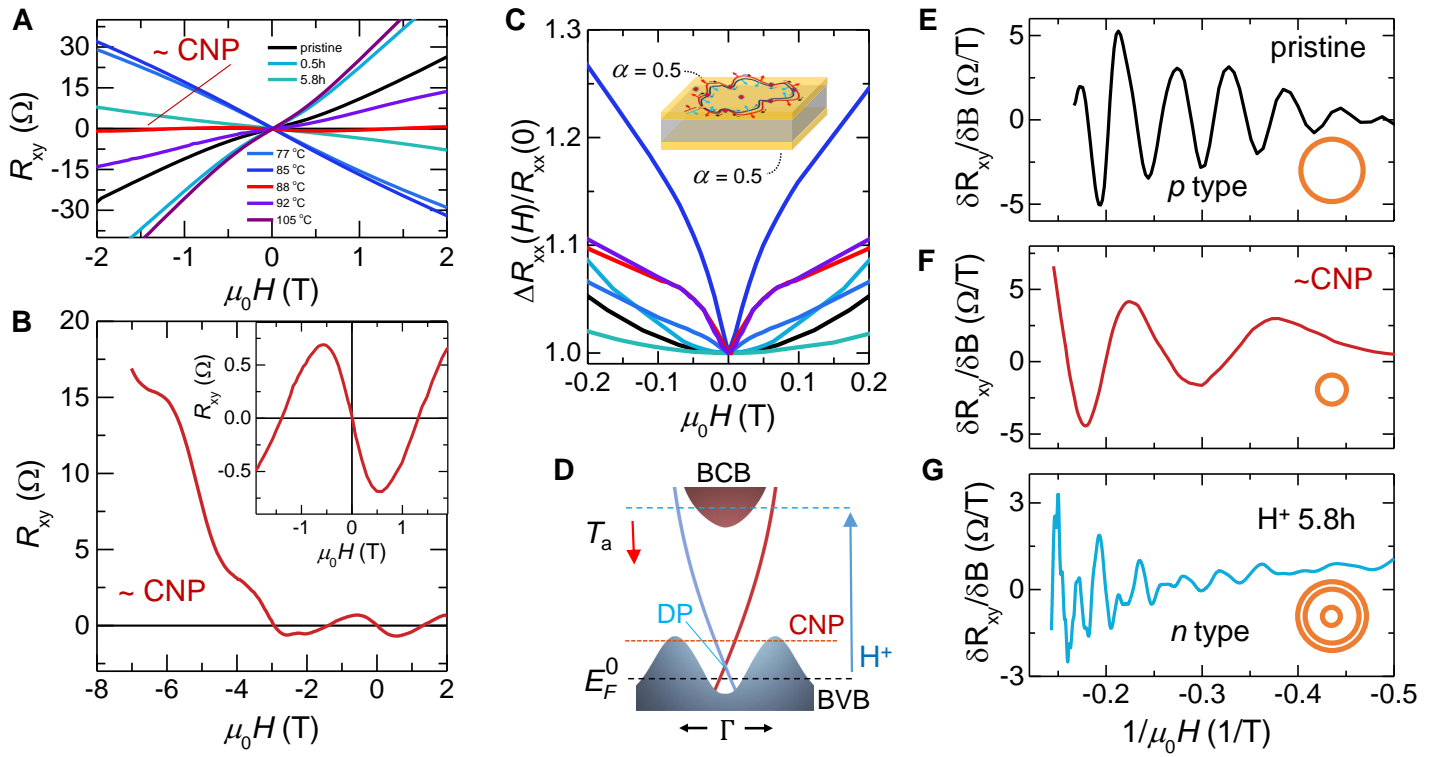


Fig. 2; HD *et al.*

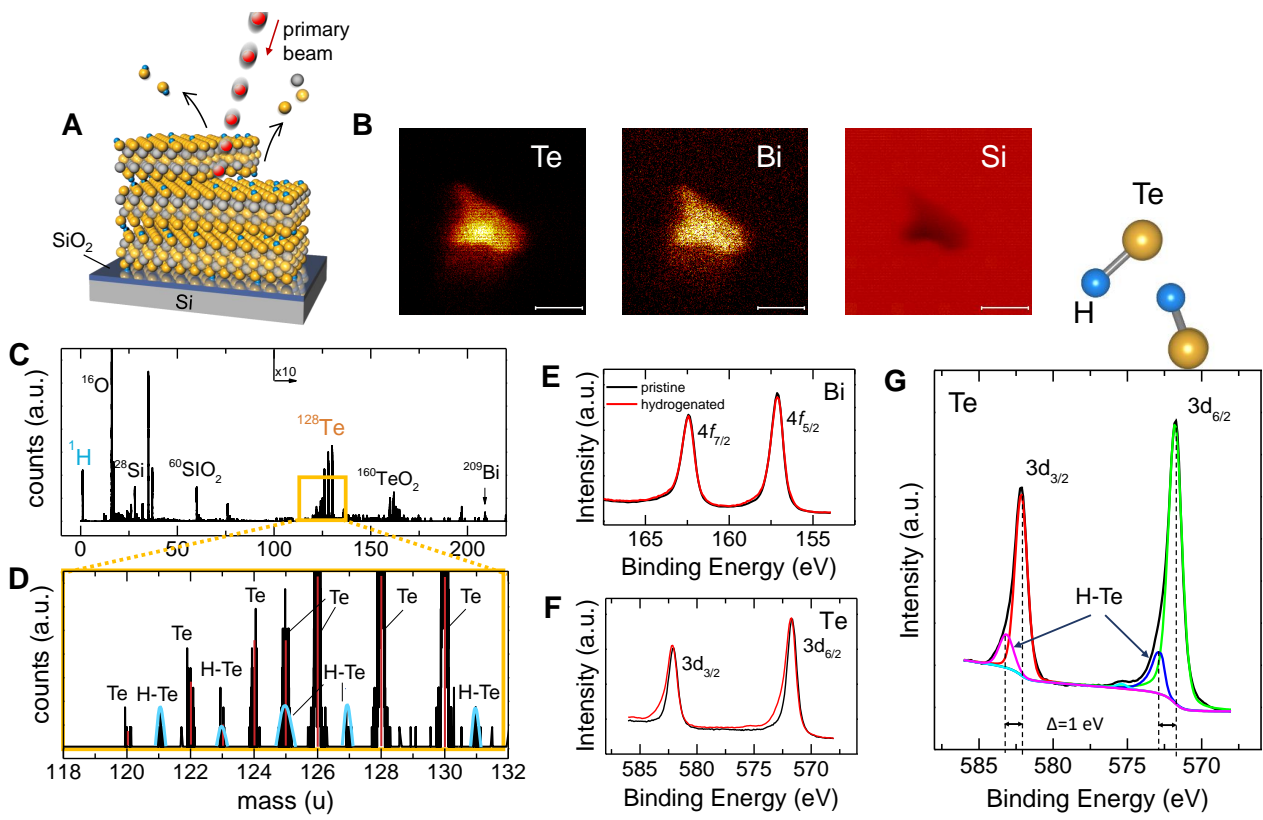


Fig. 3; HD *et al.*

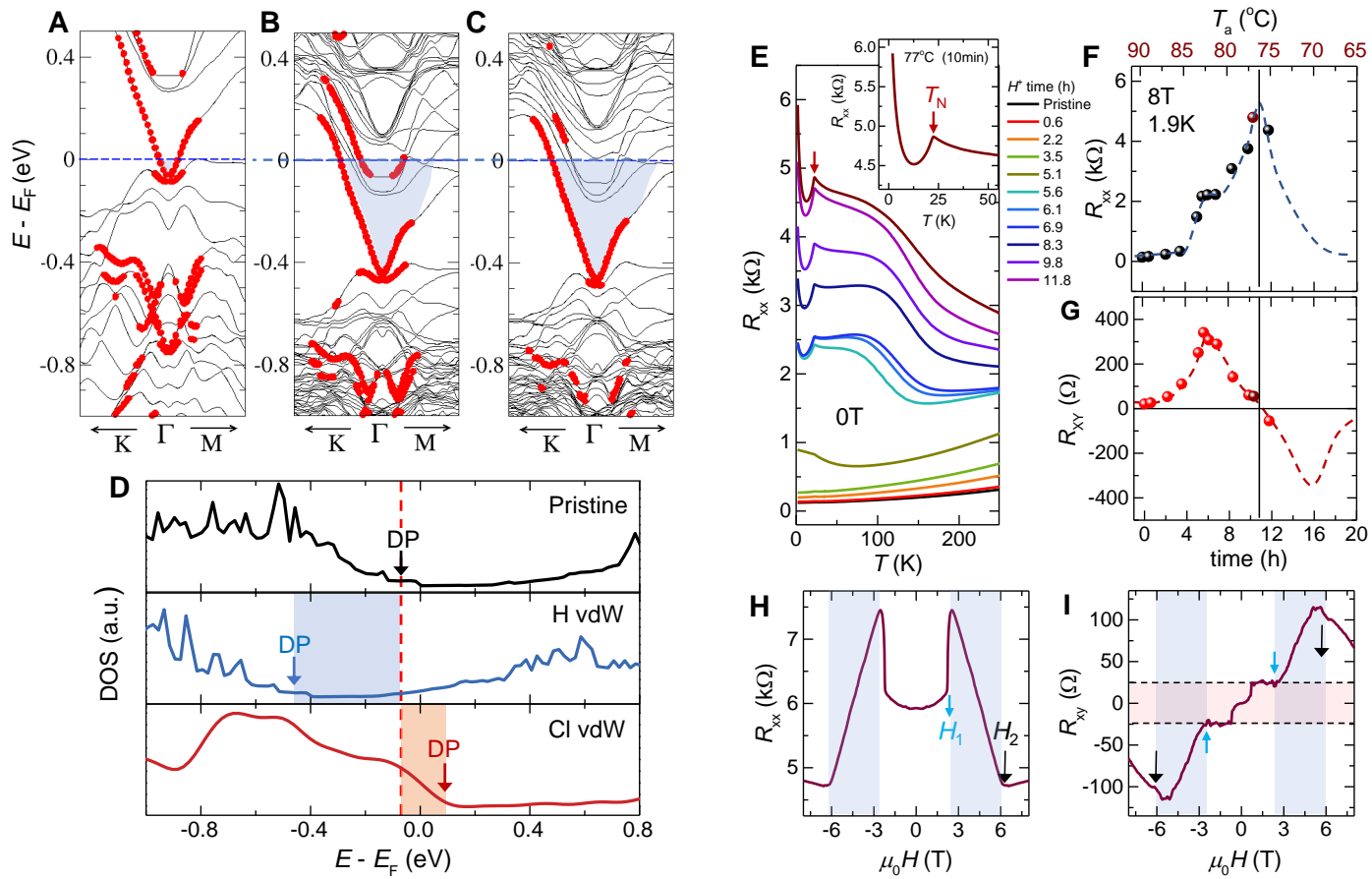


Fig. 4; HD *et al.*